Bioinspiration &
Biomimetics

PAPER • OPEN ACCESS

Magnetically-driven deployable structure inspired by worms

To cite this article: Ilaria Cedrola *et al* 2026 *Bioinspir. Biomim.* **21** 036007

Bioinspiration & Biomimetics

OPEN ACCESS

RECEIVED
13 December 2025

REVISED
14 April 2026

ACCEPTED FOR PUBLICATION
29 April 2026

PUBLISHED
13 May 2026

PAPER

Magnetically-driven deployable structure inspired by worms

Ilaria Cedrola*, Sabina Maglio, Mohammad Hasan Dad Ansari, Arianna Menciassi and Linda Paternò*

The BioRobotics Institute, Sant'Anna School of Advanced Studies, Viale Rinaldo Piaggio, 34, 56025 Pontedera, PI, Italy

* Authors to whom any correspondence should be addressed.

E-mail: ilaria.cedrola@santannapisa.it and linda.paterno@santannapisa.it

Keywords: magnetic actuation, deployable structures, sipunculid worms, soft actuation

Supplementary material for this article is available online

Abstract

This study investigates the protrusion mechanism of the unsegmented marine worm *Phascolosoma stephensoni* to inspire new actuation strategies for soft robotics. A magnetically driven, soft fluidic transmission mechanism is developed to deploy a proboscis-like structure, achieving an elongation ratio of up to 2.5 relative to the system's initial resting length. The design integrates an active fluid-filled trunk with four magnetic bending units (15 mm $\times$ 30 mm $\times$ 2 mm) and a passive proboscis housed inside during rest. Under external magnetic fields, the units compress the trunk, driving the proboscis deployment through fluid displacement, while hyperelastic passive strips enable its retraction when the magnetic field is switched off. The units were fabricated from DragonSkin-10 silicone with 5 μm NdFeB particles at concentrations ranging from 40 wt% to 70 wt%. Increasing particle content from 40 to 70 wt% yields a magnetization gain of up to $\sim$200% and marked improvements in bending performance. A trunk analytical model was developed and validated with a 2.4% error to guide the proboscis design. Final performances were evaluated in terms of proboscis displacement (up to 45 mm, i.e. a ratio of up to 2.5 relative to the system's initial resting length), internal pressure variation (up to 3 kPa), and tip force (up to 1 N). These results demonstrate how optimizing magneto-mechanical properties enables a fully soft, wirelessly actuated fluidic transmission mechanism, paving the way for applications such as targeted delivery in constrained and delicate environments.

1. Introduction

The anatomy and biomechanics of biological organisms have evolved to optimize both structure and function across a wide range of tasks. Drawing inspiration from natural systems enables the transfer of their embodied intelligence into engineered devices, paving the way for robots capable of adapting and performing more effectively in unstructured and dynamic environments [1–3]. In this context, several bioinspired designs that mimic the musculoskeletal architecture of various living beings have been proposed to enhance the adaptability and versatility of robots, enabling safe interaction with the environment as well as multiple degrees of freedom [4–7]. Among the diverse musculoskeletal designs found in nature, invertebrates have emerged as a particularly compelling source of inspiration in soft robotics, due to their use of hydrostatic skeletons that rely on internal fluid pressure to maintain shape and enable movement without the need for rigid components. By contracting muscles against the fluid, force is transmitted through internal pressure, providing structural support while allowing highly flexible and adaptable movements [8, 9]. This conversion of muscular work into force or displacement is finely modulated through the deformation of soft tissues and driven by the selective activation of muscle types specialized in either stronger or faster responses.

Among the vast class of invertebrates, worms exhibit extremely wide functional and ecological diversity in adapting and controlling movements through muscle-driven mechanical responses in their fully soft-bodied structures, thus enabling continuous interaction with the environment in response to external stimuli. However, most existing worm-inspired devices focus almost exclusively on replicating the peristaltic locomotion of segmented

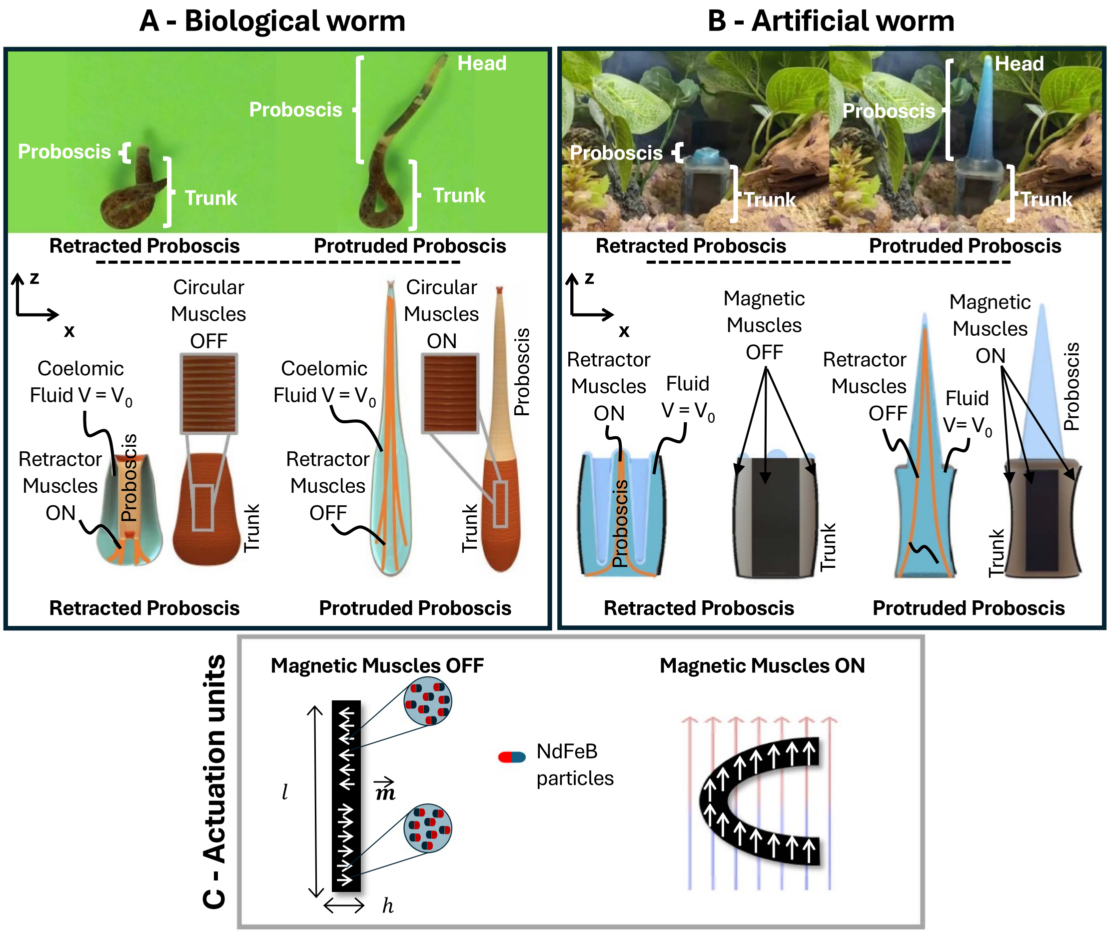

Figure 1. (A) (Top) biological worm used as a model for bioinspiration: P. stephensoni in its resting (left) and protruded (right) configurations. (Bottom) schematic of the musculoskeletal system enabling proboscis protrusion. Starting from a state in which the proboscis is retracted into the trunk due to the contraction of the retractor muscles (left), it is then protruded due to the contraction of circular muscles (right), which increase internal pressure while maintaining a constant coelomic fluid volume (V_0), thereby pushing fluid into the proboscis and driving its deployment. (B) (Top) artificial worm prototype in its initial (left) and final (right) configurations. (Bottom) schematic of the actuation strategy. The bioinspired system features a fluid-filled artificial trunk with four magnetically responsive bending units. (C) Schematic of the bending actuation units: each half of the unit (unit length = l) shows a magnetization profile m through its thickness h, but in opposite directions. This thickness-wise magnetization enables the unit to bend when an external magnetic field is applied along the +Z axis, resulting in trunk compression.

worms, involving wave-like contractions for forward crawling. To achieve this, various actuation strategies have been explored, including pneumatic [10–14], magnetic [15–18], and thermal [19, 20] actuation, shape memory alloys [21, 22] and dielectric elastomers [23]. In contrast, unsegmented worms have been much less studied, despite the fact that their continuous body structure offers greater structural flexibility and potential for novel modes of motion.

Marine *Phascolosoma (P.) stephensoni* (Sipunculidae, Annelida) is an example of an unsegmented worm which, owing to its lack of body segmentation, is capable of undergoing significant morphological change. Its body is composed of a proximal trunk and an extendable anterior structure known as the proboscis, which can be protruded during specific behaviors such as burrowing, exploration, or feeding. This protrusion mechanism arises from the synergistic action of the circular and longitudinal muscles working together with the hydrostatic skeleton, which operates without volume changes. Initially, the proboscis is fully contained within the trunk (figure 1). Then, the contraction of the circular muscles surrounding the internal fluid-filled cavity increases the coelomic pressure. This rise in pressure drives the eversion of the proboscis. Specifically, the proboscis does not simply elongate by stretching its tissues, but instead progressively unrolls outward as the internal pressure increases. When free in seawater, *P. stephensoni* exhibits the ability to reach elongation percentages ranging from 119 ± 42% to 217 ± 12% following proboscis protrusion. Notably, in an agar-based hydrogel, the worm has been observed to generate stresses of several tens of kilopascals while navigating through the medium [24].

A Sipuncula-inspired pneumatic design reported in the literature features a hollow, soft cylindrical actuator enclosed within a rigid outer shell, with a fluid-filled passive chamber at its core [25].

When the soft actuator is pressurized, it compresses the passive chamber, causing it to elongate up to ~1.5 times its initial resting length. Furthermore, the mechanism that extends the invaginated proboscis of Sipuncula outward has inspired solutions such as vine robots, in which a thin, inextensible soft tube is everted due to internal pressure, resulting in growth at the tip [26–32].

As highlighted in table 1, these solutions rely on pneumatic actuation and enable large elongation ratios at high speeds. However, they require tethered designs [26–28, 33], which lack the worms' ability to dynamically respond to environmental stimuli, and even solutions with onboard actuation result in bulky designs, with diameters on the order of 10 cm or more, making them difficult to miniaturize [34]. Conversely, smart materials offer the potential to embed responsiveness directly into the material itself, thereby overcoming the bulkiness of traditional pneumatic actuation strategies and more closely mimicking the adaptability of worms to their surroundings [35]. These materials can actively change their shape or mechanical properties in response to external stimuli such as temperature, pH, light, or magnetic fields. Importantly, some of these stimuli can be controlled remotely, enabling wireless actuation, which is a key advantage for applications in confined, hard-to-access, or delicate environments where tethered systems would be impractical.

In this scenario, magnetic actuation is particularly advantageous because magnetic fields can penetrate most materials without requiring physical contact, unlike chemical stimuli such as pH, and without line-of-sight constraints, as in light-based actuation. In addition, magnetic actuation stands out for its ability to deliver precise control, safe interaction with biological tissues, rapid response times, and high repeatability, making it a promising solution across various fields [37, 48]. Embedding hard magnetic particles within a soft matrix allows for the imposition of localized magnetization patterns, enabling anisotropic magnetization programming [38–41]. This anisotropy supports the generation of distinct motion primitives by dynamically reshaping the structure's geometry and achieving desired deformations under external magnetic fields [38, 42–44, 48].

In bioinspired robotics, soft magnetic actuation has been widely employed to develop worm-inspired systems; however, most of these approaches focus on replicating inchworm-like locomotion rather than enabling substantial axial elongation [15, 36, 40, 45, 46]. Furthermore, most of these systems integrate rigid magnets either along the body structure [15, 36] or at the distal ends [45, 46], compromising the overall softness of the structure. One of the few worm-inspired solutions capable of achieving elongation is the magnetically driven folded diaphragm reported by Lin *et al* [47]. Nevertheless, this system achieved a limited displacement of only 5 mm in prototypes with a diameter of approximately 20 mm. Aside from this example, the use of magnetic actuation in axially extendable systems has so far been limited to guiding tip bending in pneumatic vine robots [27], and its potential as a primary actuation strategy for linear motion remains largely unexplored.

In this paper, we introduce a soft robotic architecture inspired by Sipuncula worms that enables axial displacement of a proboscis-like appendage through a magnetically driven fluidic transmission mechanism. The key novelty of this work lies in the integration of magnetically responsive bending units with a fluid-filled chamber, such that external magnetic fields induce localized bending wirelessly, generating internal fluid pressure that drives linear elongation without the need for wired or cabled connections. Unlike conventional soft systems relying on pneumatic lines, rigid backbones, or tethered actuation, the proposed design converts distributed magnetic deformation into controllable axial elongation without rigid components, enabling untethered and wireless operation while preserving the intrinsic compliance of soft-bodied organisms. Particular attention is given to the architectural and material trade-offs governing performance, including stiffness gradients, magnetic responsiveness, and fluid–structure interaction. We systematically characterize the elongation behavior, defining the achievable displacement and the force output at the system's tip. The following sections provide a detailed study of the design and fabrication process, the experimental validation of the proposed smart architecture, and highlight how the synergy between magnetic actuation and optimized soft material properties enables a new fluid-pressure-based strategy for linear elongation.

2. Methods

2.1. Bioinspiration and design overview

The body of *P. stephensoni* can be divided into three main parts (figure 1(A), supplementary video 1: biological inspiration and magnetically driven proboscis eversion mechanism animation): the proximal trunk, which houses most of the muscles and internal fluids; the intermediate proboscis, which can protrude or retract into the trunk based on coelomic fluid pressure and muscle contractions; and a distal head, aligned with the trunk's orientation and typically equipped with a mouth and sensory structures. When the circular muscles in the trunk contract, reducing its circumference, they compress the coelomic fluid within the coelomic cavity of the hydrostatic skeleton. According to Pascal's principle, this compression raises internal pressure, generating a pushing force and a fluid volume displacement from the trunk into the proboscis, extending it outward. The retraction phase is powered by specialized retractor muscles that swiftly pull the proboscis back into the

Table 1. A comparative table is provided to benchmark the proposed system against the state-of-the-art in vine robots, deployable soft structures, and magnetically actuated worm-inspired robots. The comparison includes key performance metrics such as elongation ratio (defined as the ratio between the final and the initial length of the system), tip force, operating pressure, required actuation field strength, and bandwidth/speed. Additionally, the table reports whether each system relies on tethered pneumatics or rigid structural constraints.

		Max speed*	Max elongation ratio	Max force	Max actuation field strength	Tethered pneumatics	Rigid parts	Elongation
[36]	Worm-inspired magnetic robot	8.9 mm s^{-1}		0.28 N	45 mT	No	Yes	No
[15]	Worm-inspired magnetic robot	0.4 body length s^{-1}				No	Yes	No
[16]	Worm-inspired magnetic robot	1.67 mm s^{-1}		∼0.06 N	7 mT	No	No	No
[25]	Worm-inspired pneumatic robot		∼1.5	18 N	140 kPa	Yes	Yes	Yes
[26]	Vine pneumatic robot	10 m s^{-1}	700		20 kPa	Yes	Yes	Yes
[27]	Vine pneumatic robot				20.7 kPa	Yes	Yes	Yes
[28]	Vine pneumatic robot				140 kPa	Yes	Yes	Yes
[29]	Vine pneumatic robot			∼30 N	20 kPa	Yes	Yes	Yes
[30]	Growing pneumatic robot	1.490 m s^{-1}		20 N	150 kPa	Yes	Yes	Yes
[31]	Vine pneumatic robot			0.72 N	15 kPa	Yes	Yes	Yes
[32]	Vine pneumatic robot	0.309 m s^{-1}			12 kPa	Yes	No	Yes
[34]	Vine pneumatic robot	6.1 cm s^{-1}		80 N	3.45 kPa	No	Yes	No
[37]	Magnetic walking robot	∼0.25 mm s^{-1}			40 mT	No	Yes	No
[38]	Magnetic soft robots					No	No	No
[39]	Worm-inspired magnetic robot		0.35		90 mT	No	No	No
[40]	Worm-inspired magnetic robot				80 mT	No	No	No
[41]	Magnetic walking robot	2 mm s^{-1}	0.5		∼250 mT	No	No	No
[42]	Magnetic walking robot	15 mm s^{-1}			30 mT	No	No	No
[43]	Magnetic walking robot	2.46 mm s^{-1}			13 mT	No	No	No
[44]	Magnetic walking robot	2.7 mm s^{-1}			50 mT	No	Yes	No
[45]	Worm-inspired magnetic robot	12 mm s^{-1} (5 Hz)			12 mT	No	Yes	No
[46]	Magnetic walking robot			0.29 N		No	Yes	No
[47]	Worm-inspired magnetic robot		5 mm displacement	0.8 N	40 mT	No	No	Yes
Our work	Everting robot	90 mm s^{-1}	2.5	0.95 N	250 mT	No	No	Yes

* Max speed refers to elongation speed for systems relying on linear elongation and to locomotion speed for systems that move via crawling.

trunk when contracted, enabling rapid retraction for protection.

Like its biological counterpart, the proposed solution includes a fluid-filled artificial trunk and a deployable proboscis-like structure, on which a sensor or an agent to be released can be integrated (figure 1(B)). The trunk measures 30 mm in length and exhibits a slightly bulged design with an aspect ratio ($L/D \approx 1.5$), approximately half that of sipunculid worms, which typically display trunk lengths of around 12 mm and diameters of about 4 mm ($L/D \approx 3$). This design configuration was selected to simplify fabrication and enhance structural stability under internal pressure.

During the design process, the mechanical properties and magnetic responsiveness of soft materials were strategically exploited to develop a fully soft system capable of responding to magnetic stimuli and wirelessly deploying its internal proboscis through hydrostatic pressure. Specifically, the trunk wall was fabricated from an ultra-soft silicone (EcoFlex-0010, Shore hardness: 00–10), incorporating four 15 mm $\times$ 30 mm regions with a thickness of 2 mm composed of a stiffer silicone (DragonSkin-10, Shore hardness: 10 A) embedded with 70 wt% of NdFeB hard magnetic microparticles (average particle size: 5 μm). These materials were carefully selected to ensure that the trunk wall remained highly deformable, offering minimal resistance to the motion of the magnetic bending units, while the embedded segments provided increased actuation force thanks to their higher stiffness, density, and magnetization. The embedded regions function as actuation units that mimic the role of circular muscles in biological worms through targeted magnetization programming. Specifically, their magnetization direction causes them to fold inward under an external magnetic field aligned with the $+Z$ axis, which leads to a reduction in trunk volume and compression of the enclosed fluid ($\sim$20 ml of water). This deformation generates hydrostatic pressure that drives the axial deployment of the inner proboscis, effectively converting magnetic input into linear extension without requiring rigid components or tethered actuation. An ultra-stiff silicone (Smooth-Sil 960, Shore hardness: 60 A) was used to reinforce the trunk base, as its high stiffness provides mechanical support and structural stability during actuation. The passive proboscis is a 45 mm long, cone-shaped structure designed to accommodate nearly all the fluid displaced by the magnetic artificial muscles. It is fabricated from an ultrathin (200 μm) layer of ultra-stiff silicone (Smooth-Sil 950, shore hardness: 50 A), which remains compliant while providing the structural rigidity necessary to prevent undesired radial expansion under internal fluid pressure.

When fully deployed, the proboscis enables the system to achieve an elongation ratio of up to 2.5 times its initial resting length, closely mimicking the morphological changes observed in sipunculid worms. Specifically, the elongation ratio ($\lambda_{\text{structure}}$) is defined as:

$$\lambda_{\text{structure}} = \frac{L_f}{L_0}$$

where L_f is the final length of the soft robotic structure (75 mm), and L_0 is the initial length of the soft robotic structure (30 mm) (table 2), corresponding to the final and initial configurations shown in figure 1(B), respectively. Specifically, the initial length is defined as the height of the soft robotic structure when no magnetic field is applied. In this initial configuration, the trunk is not compressed by the magnetic bending units, and the proboscis is retracted within the trunk. Conversely, the final configuration occurs when an external magnetic field actuates the bending units in the trunk, compressing it and forcing the complete protrusion of the proboscis. All lengths are referenced along the centerline of the structure.

To replicate the retraction mechanism provided by retractor muscles in Sipuncula worms, two passive ultra-soft silicone strips (EcoFlex-0010, Shore hardness: 00–10) measuring 20 mm $\times$ 2 mm with a thickness of 400 μm were symmetrically fixed from the distal tip of the proboscis to the base of the trunk. These strips act as elastic restoring elements that, once the magnetic field is decreased, generate a retraction force sufficient to drive the rapid and complete withdrawal of the proboscis into the trunk, thus completing the actuation cycle.

2.2. Actuation units

2.2.1. Material characterization

Magnetic and mechanical properties of the material employed for the actuation units were investigated. To assess the impact of material composition on actuation performance and manufacturability, four different concentrations of hard magnetic particles (40 wt%, 50 wt%, 60 wt%, and 70 wt%) were evaluated using DragonSkin-10 (D10) silicone as the polymer matrix. Although higher magnetic particle loadings were initially explored, concentrations above 70 wt% were found to introduce significant processing challenges. In particular, increasing particle content made it difficult to achieve uniform dispersion within the silicone matrix, leading to local variations in magnetic and mechanical properties that compromised actuation consistency. Higher particle concentrations required substantially longer mixing times to reach acceptable homogeneity. The extended mixing process increased the temperature of the composite, inducing partial premature curing of the silicone matrix prior to deposition with the film applicator used to produce 1 mm thick layers. These effects resulted in defects, non-uniform thicknesses, and less reproducible actuation performance. For these reasons, particle loadings above 70 wt% were not considered practically viable.

Table 2. List of the geometrical and experimental parameters used in the design, modeling, and characterization of the magnetically driven deployable structure throughout the manuscript.

Symbol	Description
a	Corner width
b	Bulged state
cc	Concave configuration
cv	Convex configuration
w	Width of the central trunk region
α	Half-angle of the bending arc
θ_{cc}	Bending angle in the concave configuration
θ_{cv}	Bending angle in the convex configuration
V_o	Volume of the trunk in its steady state
r	Curvature radius of the bulged units
h_b	Height of the trunk in its steady state
t	Arc length of the actuated bending unit
A_b	Bending area
ΔV_{cc}	Change in volume in the concave configuration
ΔV_{cv}	Change in volume in the convex configuration
L	Bending unit length
h	Bending unit thickness
L_0	Initial length of the structure
L_f	Final length of the structure
λ_{mat}	Elongation ratio of hyperelastic silicone material
$\lambda_{structure}$	Elongation ratio of the soft robotic structure
M	Magnetization (i.e. the magnetic moment density per unit volume)
m_1	Magnetic moment
B_m	Magnetic field for magnetizing
B_a	Actuation magnetic field
α	Bending angle
v_1	Vector between end points of the reconstructed skeleton
v_2	Vector along the length of the actuated unit
$\rho_{silicone}$	Silicone density
ρ_{mix}	Composite density (NdFeB particles + silicone)
ω	Mass fractions
σ	Nominal stress of hyperelastic silicone material
σ_m	Saturation magnetization per unit mass
μ_p, α_p	Ogden material parameters
F_m	Magnetic force
τ_m	Magnetic torque

Mechanical properties of the soft magnetic composite were evaluated by performing tensile tests in accordance with the ISO 37:2024 standard, which specifies methods for determining the tensile stress–strain properties of elastomeric materials. The tests were conducted using a uniaxial testing machine (Instron 5695, Instron) with a 1 kN load cell. Dumbbell-shaped samples were prepared and then tested. Each test involved 50 deformation cycles at a deformation speed of 200 mm min^{-1}. The tensile test results were obtained by testing five samples for each silicone–magnetic particle combination, i.e. D10–40 wt%, 50 wt%, 60 wt%, and 70 wt%.

Before performing the cyclic tensile tests, three specimens for each combination of silicone and magnetic particles under investigation underwent a breakage test, and the corresponding elongation was measured. As expected, the most rigid sample (D10–70 wt%) showed the lowest strain at break, equal to 350%. This value was taken into account as a benchmark for performing cyclic tests, which were carried out by setting a maximum strain of 100%. This test allowed the investigation of a deformation range substantially larger than that expected in the target application while still remaining sufficiently below the failure threshold to avoid specimen breakage during testing.

The resulting stress–strain curves were fitted in MATLAB using the Ogden hyperelastic model. Under the assumptions of uniaxial stress conditions and an incompressible, isotropic material, the Ogden model defines the nominal stress (σ) of a hyperelastic material as a function of the elongation ratio (λ_{mat}, defined as the ratio between the final and the initial length of the sample) and the material parameters, μ_p and α_p, using the following equation:

$$\sigma = \sum_{p=1}^{N} \mu_p \left({\lambda_{mat}}^{\alpha_p - 1} - {\lambda_{mat}}^{-\left(\frac{\alpha_p+2}{2}\right)} \right). \quad (1)$$

Then, the vibrating sample magnetometer (Microsense, EZ9, USA) was employed to quantify the magnetization of each silicone magnetic particles combination. The samples were cut in a squared shape (2 mm × 2 mm × 1 mm). The magnetic moment (m_1) along the magnetization direction were measured on five samples for each silicone magnetic particles combination and then averaged across the samples. The magnetization M (i.e. the magnetic moment density per unit volume) was evaluated considering the magnetic composite density (ρ), as follows:

$$M\left[\frac{A}{m}\right] = \sigma_m \left[\frac{A \cdot m^2}{Kg}\right] \rho_{mix} \left[\frac{Kg}{m^3}\right] \quad (2)$$

where ρ_{mix} indicates the density of the composites and σ_m indicates the saturation magnetization per unit mass, which was calculated from the magnetic moment by dividing by the sample mass. The mass was measured using a Quintix® analytical balance (Sartorius Lab Instruments GmbH, Germany). To estimate the overall density of the composite material, composed of a silicone matrix and dispersed NdFeB particles, the rule of mixtures was applied based on mass fractions. When the composition is defined in terms of weight percentage, the effective density ρ_{mix} of the two-component system can be calculated using the following inverse relation:

$$\frac{1}{\rho_{mix}} = \frac{\omega_{silicone}}{\rho_{silicone}} + \frac{\omega_{NdFeB}}{\rho_{NdFeB}} \quad (3)$$

where $\omega_{silicone}$ and ω_{NdFeB} are the mass fractions of the silicone and NdFeB particles, respectively, and $\rho_{silicone} = 1.08$ g cm^{-3} and $\rho_{NdFeB} = 7.61$ g cm^{-3} are their corresponding densities. This approach was applied to composites containing 40 wt%, 50 wt%, 60 wt%, and 70 wt% of NdFeB particles.

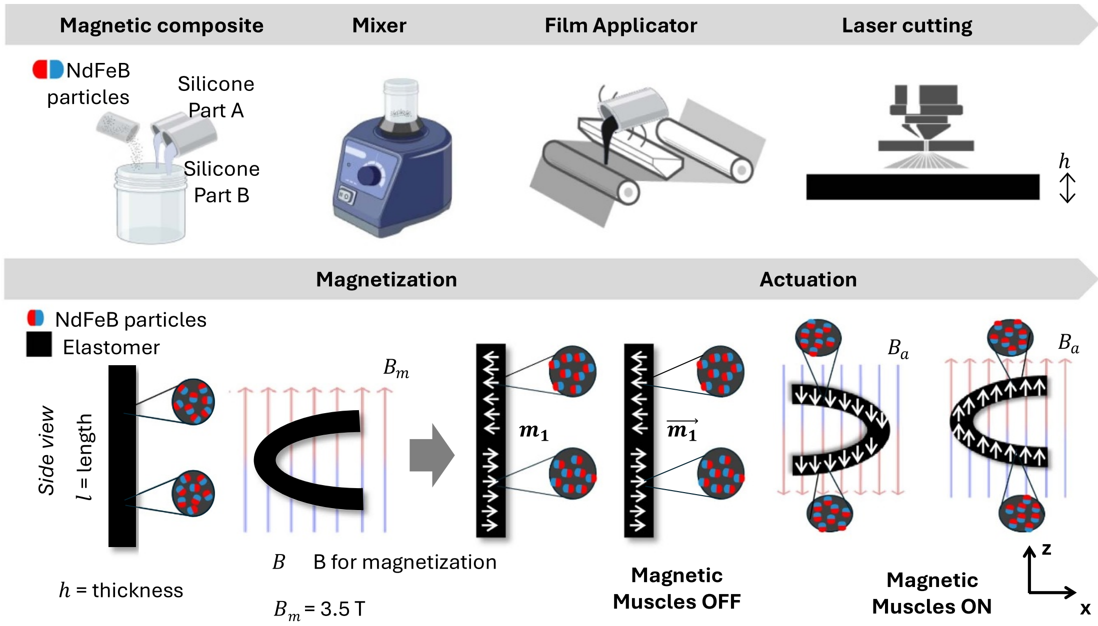

Figure 2. Magnetic bending actuation units function as artificial muscles within the proposed system. These units are fabricated by mixing silicone with magnetic particles and forming films of the desired thickness h using a manual film applicator. The films are then laser-cut into rectangular shapes. The resulting layers are magnetized in a folded configuration using a magnetizer that applies a magnetic field of 3.5 T along the +Z-axis. As a result, the actuation units bend in response to an external magnetic field.

2.2.2. Bending performances

As detailed in figure 2, the magnetic bending actuation units were characterized by a thickness-wise magnetization profile. Specifically, each unit consists of two halves with opposing magnetization directions (one side magnetized positively and the other negatively). In this way, under an external magnetic field applied along the Z-axis, the misalignment between the field direction and the internal magnetization induces a bending torque, producing either concave or convex curvature depending on the orientation. Consequently, a magnetic body with a magnetic moment (m_1) placed in a magnetic field (B_a) experiences a magnetic force (F_m) and a magnetic torque (τ_m), as given by equations (4) and (5), respectively:

$$F_m = \nabla (m_1 \cdot B_a) \tag{4}$$

$$\tau_m = m_1 \times B_a. \tag{5}$$

For the manufacturing of the actuation units (supplementary video 2: fabrication and magnetization process of the actuation units), DragonSkin-10 silicone was prepared by mixing parts A and B at a 1:1 weight ratio. NdFeB microparticles (average particle size: 5 µm; MQP-15-7-20065, Magnequench) were then added at 70 wt% and homogeneously dispersed in the mixture using a planetary mixer (IGT SimplyMix), after which the composite was degassed for 1 min.

A 1 mm thick composite sheet was then fabricated using a film applicator (Zehntner GmbH Testing Instruments, Switzerland) and left to cure overnight at room temperature. Then, rectangular bending units (15 mm × 30 mm) were laser-cut and subsequently folded and magnetized using an impulse magnetizer (MAGNET-PHYSIK T-SERIES MF-AsA-ø25.0 × 60.0 mm-1218). Magnetization was performed using a single magnetic field pulse with a peak intensity of $B_m = 3.5$ T to establish the desired magnetization profile. The bending units were designed to deform along their longitudinal direction l (figure 1(C) and 2). Thus, during the magnetization process, they were folded lengthwise and magnetized through the thickness h. As a result, the applied magnetic field was oriented perpendicular to the thickness direction of the actuation units. A simple field-alignment jig was used during magnetization. Two square supports were employed to maintain the desired orientation of the samples with respect to the applied magnetic field, thereby minimizing misalignment and ensuring consistent magnetization across specimens (see supplementary video 2: fabrication and magnetization process of the actuation units).

For each composite concentration, the bending performance was experimentally evaluated using a commercial 8-coil electromagnetic field generator (Magneticbox). The applied magnetic field was controlled in open loop through the system's software interface. Tests were conducted under varying external magnetic field strengths ($B_a = 10$ mT, 30 mT, and 50 mT). Due to design symmetry, only half of each bending unit was tested. Each test condition was repeated five times on five different samples.

Images of the actuated bending units were captured and processed in MATLAB. Specifically, the extraction of the bending unit's skeleton enabled the identification of the end points, thus allowing the calculation of the bending angle α. Defining v_1 as the vector between the end points and v_2 as the vector along the length of the unactuated unit (see figure 5 in the results section), the bending angle α was calculated as:

$$\alpha = \frac{180 - \left(\frac{cos(v_1 \cdot v_2)^{-1}}{||v_1||*||v_2||}\right)}{2}. \quad (6)$$

2.3. Artificial trunk

The artificial trunk was conceived as a fluid-filled, bulged square prism ($b = 2$ mm) structure integrating four bending units, one on each side. Its optimal design was investigated to guide the subsequent development of the proboscis, based on the maximum volume of fluid that can be displaced during actuation. A geometrical–analytical model was developed to evaluate the variation in trunk volume during actuation. Figure 3 presents the geometrical parameters used in the model. The prototype deflection at the rounded edges was not taken into account in the model. The volume of displaced fluid depends on the bending direction of the units, which can form either a convex or concave shape.

In a steady state, when no magnetic field is applied, the initial trunk volume V_0 is calculated by considering two contributions, namely the volume of the trunk without considering the bulged region (V_1) and the volume of the bulged region (V_2):

$$V_1 = \left[(w + 2 \cdot a)^2 + \pi * a^2 - 4 * a^2\right] \cdot h_b \quad (7)$$

$$V_2 = \frac{1}{2}\left[4 * {r_b}^2 * 2 * \alpha_b * w - 4 * h_b * t_{1b} * w\right]. \quad (8)$$

Due to the bulged configuration, a circular arc is formed by the bending units, and r_b corresponds to its radius, while $t_{1b} = r_b * \cos(\alpha_b)$, as shown in figure 3(A). The theoretical initial trunk volume V_0 was found to be approximately 20 ml.

When the bending units bend inwards, a concave configuration is obtained (figure 3(B)).

In this configuration, the bending units form a circular arc with radius r_{cc} when actuated and exhibit a bending limit, as the units begin to interfere with each other beyond a certain internal deflection. Considering a circular sector of radius r and an arc length equal to t, we assume that:

$$t_{1cc} = r_{cc} cos\alpha \quad (9)$$

$$r_{cc} = t_1 + a \quad (10)$$

$$a = r_{cc} cos(\pi - \alpha) \quad (11)$$

$$t_{2cc} = r_{cc} sin\alpha \quad (12)$$

$$h_{cc} = 2\, t_2. \quad (13)$$

The application of the magnetic field results in a change in the prototype volume ΔV_{cc}:

$$\Delta V_{cc} = V_0 - V_{fcc} \quad (14)$$

where the volume $V_{fcc} = V_{1cc} - V_{2cc}$ represents the trunk volume in the actuated configuration. The volume V_{1cc} corresponds to the volume of the square prism after the height change (h_{cc}), while V_{2cc} is the volume of the four lateral bulged regions, each with a radius of $c = 5$ mm:

$$V_{1cc} = \left[(w + 2 \cdot a)^2 + \pi * a^2 - 4 * a^2\right] \cdot h_{cc} \quad (15)$$

$$V_{2cc} = \frac{1}{2}\left[4 * {r_{cc}}^2 * 2 * \alpha_{cc} * w - 4 * h_{cc} * t_{1cc} * w\right]. \quad (16)$$

When the bending units bend outward (figure 3(C)), a convex configuration is achieved, and the change in volume depends on the degree of bending (θ_{cv}), is there is no interference between layers. For smaller bending, the bending units bulge outward and can be assumed to take the shape of an arc. However, for larger bending, the units are observed to bend into a V-shape, and therefore the volume calculation is based on a V-shape. The trunk volume in the actuated configuration is:

$$\Delta V_{cv} = V_0 - V_{fcv} \quad (17)$$

where the induced volume change ($V_{fcv} = V_{1cv} + V_{2cv}$) can be calculated considering the volume change related to the height change (h_{cv}), while V_{2cv} is equal to the volume of the bulged region

$$V_{1cv} = \left[(w + 2 \cdot a)^2 + \pi * a^2 - 4 * a^2\right] \cdot h_{cv} \quad (18)$$

$$V_{2cv} = \frac{1}{2}\left[4 * h_{cv} * d_{cv} * w\right] \quad (19)$$

where the values of h_{cv} and d_{cv} were calculated as follows:

$$h_{cv} = h_b \cos(\theta_{cv}) \quad (20)$$

$$d_{cv} = \frac{h_b}{2} \sin(\theta_{cv}). \quad (21)$$

The analytical model was experimentally validated through a set of tests to assess the amount of fluid that the bending units can displace under both directions of the magnetic field (supplementary video 3: volume-change assessment for proboscis design). Specifically, prototypes were built consisting of the trunk structure and a non-deformable chamber placed above it to collect the internal fluid displaced when the actuation units bend either into a concave or convex shape, allowing the assessment of trunk volume change. In this way, the change in the fluid height (Δh) was measured, and the

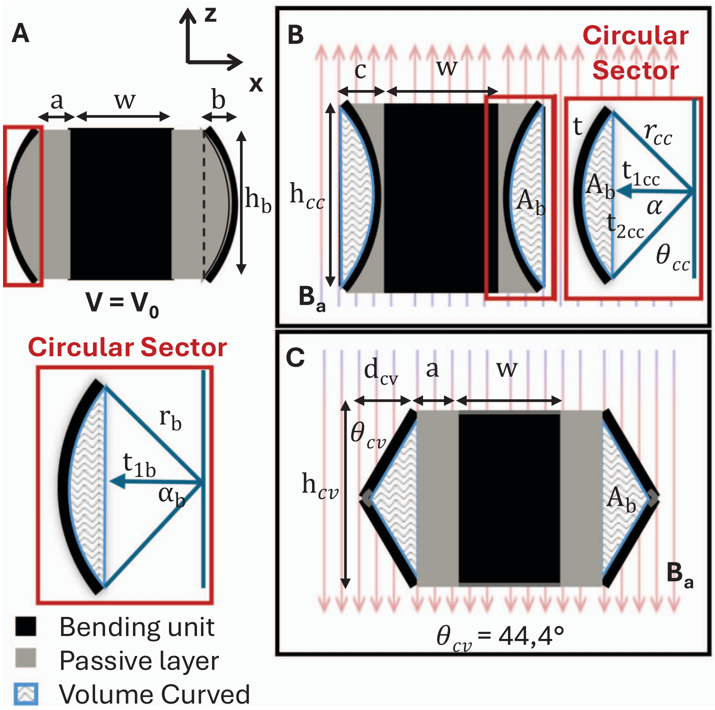

Figure 3. Geometrical model developed to evaluate trunk volume variation during actuation. (A) In the resting state, the actuation units are bulged (b = 2 mm). Upon application of the magnetic field, the bending units respond to the stimulus, causing the squeezing of the trunk. Depending on the direction of the magnetic field, either a (B) concave or (C) convex configuration can be achieved.

volume change was calculated as $\Delta V = A * \Delta h$. During the tests, the external magnetic field increased up to 150 mT. Beyond this value, both configurations collapsed onto themselves, preventing further comparison. As the volume change in the convex configuration strongly depends on θ_{cv}, it was experimentally measured at 150 mT for properly calculating the theoretical volume, and it resulted in 44°.

Tests were first conducted on trunk prototypes incorporating 1 mm thick bending units. To further increase the displaced fluid volume in the concave configuration, additional tests were performed on prototypes in which the 1 mm thick bending units were modified by incorporating a groove along the bending line, where the thickness was reduced from 1 mm to 0.5 mm. The groove acts as a mechanical discontinuity that locally reduces stiffness, thereby facilitating bending capability under magnetic actuation. Then, the thickness of the grooved bending units was increased to 2 mm, thereby increasing the amount of magnetic material incorporated. Based on the obtained results, grooved bending units with a thickness of 2 mm were fabricated and integrated into the final trunk prototypes to enhance fluid displacement capacity for proboscis actuation. While the bending units used for initial bending tests were produced using a film applicator, the grooved bending units require the use of a dedicated mold.

Knowing the amount of fluid volume that the trunk can displace in a concave deformation, the proboscis was subsequently designed as a conical structure with a total volume equal to 35% of the trunk volume. This value, slightly lower than the maximum displaced volume, was selected to optimize system performance, ensuring reliable fluid transfer while improving the efficiency of force generation during actuation.

2.4. Manufacturing

The artificial trunk was manufactured using a molding technique, resulting in a continuous hollow structure with four magnetically responsive bending units and passive interconnection areas made of 1 mm thick E10 silicone. The bottom wall of the trunk was then reinforced with a 1 mm thick layer of Smooth-Sil 960 silicone. The mold was designed using Autodesk Fusion 360® (Autodesk Inc.) and included an inner body and an external shell where the bending units were positioned. The inner body was designed with a height of 30 mm and a rounded square shape with a radius of 4 mm.

Designed as a passive, cone-shaped structure, the proboscis was made of Smooth-Sil 950 diluted with 35% NOVOCS™ Matte (Smooth-On Inc.) by volume. A dip-coating technique was employed to create a thin-walled structure of 200 µm. The proboscis was cured in an upside-down position to allow the silicone to flow downward, resulting in a very thin final wall thickness.

After curing both the trunk and the proboscis, the hyperelastic strips were attached to the worm-inspired structure. Two strips, fabricated from E10 silicone, were fixed at one end to the base of the trunk and at the other end 5 mm from the tip of the proboscis. E10 silicone was selected for its high stretchability; during eversion, it did not significantly limit the deployment of the proboscis, while its spring-like behavior facilitated its retraction. The strip dimensions played a crucial role in achieving an optimal trade-off between these two behaviors. The elastic strips were cast with a thickness of 0.4 mm, a length of 20 mm, and a width of 2 mm.

Finally, the worm-inspired structure was sealed using silicone glue, and 17.5 ml of water was introduced into the trunk via a syringe as the internal fluid.

2.5. Performance characterization

To assess the performance of the final worm-inspired soft structure, a N35 grade cylindrical external permanent magnet (EPM, outer diameter = 60 mm, inner diameter = 10 mm, length = 70 mm) was employed as a magnetic field source. The EPM was modeled as a magnetic dipole with magnetic moment m_2 (for $r > 2$ cm). Then, the magnetic field $B_\mathrm{a}(r)$ produced by the dipole is [49]:

$$B_a(r) = \frac{\mu_0}{4\pi}\left(\frac{3r(m_2 \cdot r)}{r^5} - \frac{m_2}{r^3}\right) \tag{22}$$

where r denotes the displacement vector from the center of the permanent magnet to the point at which the field is calculated, and μ_0 is the dipole permeability constant.

In the experimental setup, the intensity and direction of the magnetic field applied along the Z-axis were modulated by adjusting the pose of the EPM through a robotic positioning system controlled in open loop. The field strength ranged from 10 mT (corresponding to $r = 95$ mm from the EPM) to 250 mT ($r = 5$ mm from the EPM) and was measured using a 3-axis Hall-effect magnetic sensor (TLE493D-W2B6, Infineon). To characterize the relationship between magnetic field intensity and distance from the EPM, measurements were repeated five times, and the mean $\pm$ standard deviation values are reported in figures 6(A)–(I) (maximum standard deviation equal to 2.17 mT). During these measurements, the Hall-effect sensor was fixed at the same position as the bottom base of the worm-inspired prototype during the experiments, while the magnet was moved using a robotic arm (Melfa RV-3S, Mitsubishi, Japan), starting from an initial distance of $r = 95$ mm from the sensor. The magnetic field was continuously recorded as the magnet approached the sensor. The distance between the EPM and the sensor was controlled in open loop through the robotic arm position control software (RT ToolBox3, Mitsubishi, Japan), and the magnet was progressively moved until the distance reached $r = 5$ mm.

Tests were carried out using prototypes with and without passive retractor muscles to evaluate their influence on the overall actuation performance and to assess whether the inclusion of these elements could influence the stability of the structure. Three samples were manufactured and tested for each configuration (with and without retractor muscles). Each sample was tested three times, and the resulting values were averaged to calculate the mean and standard deviation, enabling assessment of variability associated with the manufacturing process. Specifically, the ability of the proposed solution to deploy the proboscis-like structure in a controlled manner was assessed by tracking its tip while increasing and decreasing the magnetic field, using the experimental setup in Figure S1A of the supplementary materials. Tip tracking was used to evaluate the proboscis displacement, defined as the axial distance travelled by the proboscis tip during protrusion. The initial length (L_0) corresponds to the height of the soft robotic structure in its initial configuration, i.e. in the absence of an applied magnetic field, when the proboscis is retracted inside the trunk (figure 1(B), left). At different stages of protrusion, the current length L was recorded, and the proboscis displacement was calculated as the difference between the current length and the initial length ($L - L_0$), until reaching the final length of 75 mm (L_f), corresponding to a maximum proboscis displacement of 45 mm. All displacement measurements refer to the central longitudinal axis of the structure. The analysis included tip tracking along the vertical (Z) direction, corresponding to the eversion motion, as well as within the Z–X plane to assess potential lateral oscillations of the tip during actuation, using a custom MATLAB code (MathWorks, R2023). Tip tracking was performed through a color-based segmentation strategy in the HSV (hue, saturation, value) space. Each frame of the video was cropped to include only the area of interest and converted to HSV; the pixels were then thresholded based on their proximity to the reference values for hue, saturation, and value. To improve robustness, the search area in each frame was constrained to a circular neighborhood centered on the previously detected tip location. Morphological filtering was then applied to remove noise and close small gaps, and the tip position was identified as the uppermost pixel within the segmented region. This frame-to-frame detection with spatial constraints enabled reliable tracking of the tip trajectory, which was subsequently converted from pixels to physical units.

To monitor internal fluid pressure variations, an MPXV4006 (NPX) pressure sensor was mounted at the base of the prototype and connected to a needle inserted into the device during actuation (figure S1(A), supplementary materials). Data were acquired using a DAQ system (USB-6009, National Instruments) controlled via LabVIEW.

In a second set of tests, pressure was measured simultaneously with tip force at different proboscis displacements, ranging from 5 mm to the maximum of 45 mm, using the experimental setup in figure S1(B) of the supplementary materials. The experimental setup included a 5 N load cell (FS09, Inelta Sensorsysteme GmbH & Co.) connected to a data acquisition system (USB-6009, National Instruments), operated via LabVIEW for signal recording (figure S1(B), supplementary materials). In all experimental tests, the prototype was positioned vertically under gravity on a rigid horizontal plastic sheet. The device was unconstrained, with the only boundary condition being frictional contact between its base and the supporting plastic sheet. Protrusion occurred freely in air, without mechanical guidance or axial or lateral confinement. During all the performance characterization experiments, the speed of the EPM was maintained at 50 mm s^{-1}. Additional details on the experimental setup are provided in the supplementary materials.

2.6. Dynamic characterization

To assess the ability of the final worm-inspired soft structure to evert and retract its proboscis under dynamic conditions, tests were performed by actuating the system at different magnetic field strengths. The N35 EPM was mounted as the end effector of a robotic arm (Doosan Robotics, Suwon, South Korea), whose motion speed was controlled to enable modulation of the magnetic actuation frequency. Three different magnet distance frequency values were tested, namely $f_1 = 0.5$ Hz, $f_2 = 0.6$ Hz, and $f_3 = 0.8$ Hz. The dynamic response under these conditions was evaluated by tracking the motion of the proboscis tip during both protrusion and retraction phases. As in the performance characterization tests described above, the tip position was tracked using a custom MATLAB code (MathWorks, R2023) based on a color-based segmentation strategy in the HSV (hue, saturation, value) space.

3. Results

3.1. Actuation units

The stress–strain curves resulting from tensile tests at break, conducted on dog-bone specimens using an Instron testing machine, are reported in figure 4, while those from cyclic tensile tests fitted using the Ogden hyperelastic model are shown in figure 5(II). The Ogden model parameters (μ_p and α_p in equation (1) of each silicone–magnetic particle combination are reported in table 3. The mechanical characterization of the composites revealed a progressive increase in stiffness with higher particle content. As stiffness increased, the specimens exhibited failure at lower strains during tensile tests at break (figure 4). Nevertheless, even at the highest particle concentration (70%), failure strains remained above 3 (i.e. a strain greater than 300%), which is far beyond the strain levels expected in the proposed design and therefore does not pose a limitation for the intended application.

Magnetization measurements are reported in figure 5(III). Based on equation (3), the estimated densities of the composites were found to be 1.64 g cm^{-3} for 40 wt% NdFeB, 1.89 g cm^{-3} for 50 wt%, 2.21 g cm^{-3} for 60 wt%, and 2.71 g cm^{-3} for 70 wt%. Using the estimated densities together with the saturation magnetization values, the magnetization M was then calculated using equation (2).

The bending angle achievable by the actuation units can be seen in figure 5(I). As expected, the achievable bending angle was found to strongly depend on the magnetic field strength and the concentration of hard magnetic particles embedded in the composite structure. Indeed, the magnetization properties of the material depend on two key factors: the concentration of hard magnetic particles and the elastomer density. Higher values of these factors result in higher magnetization. This highlights the importance of optimizing the balance between mechanical compliance and magnetic responsiveness to achieve high-performance, magnetically actuated soft structures.

Notably, increasing the particle content from 40 wt% to 50 wt% results in a pronounced enhancement in bending performance, with an average increase of approximately 44%, 16%, and 13% in bending angle at 10 mT, 30 mT, and 50 mT, respectively. This enhancement correlates with a substantial gain in magnetization (from 6.75×10^4 A m^{-1} at 40 wt% to 9.70×10^4 A m^{-1} at 50 wt%), while the mechanical stiffness remains similar, highlighting the role of magnetic responsiveness in driving actuation. Further increasing the particle content to 60 wt% yields only marginal gains in bending performance despite a continued increase in magnetization. This indicates a potential saturation effect, where the benefits of enhanced magnetization are offset by the modest increase in stiffness, which begins to hinder deformation. However, at 70 wt%, a marked improvement in bending angle is again observed across all field strengths, suggesting that beyond a critical loading threshold, the enhanced magnetic responsiveness (magnetization equal to 1.26×10^5 A m^{-1} at 60 wt% and 2.04×10^5 A m^{-1} at 70 wt%, figure 5(III)) is sufficient to overcome the mechanical constraints imposed by the stiffer composite. Based on these results, a 70 wt% concentration was identified as the optimal choice, combining superior bending performance with preserved manufacturability.

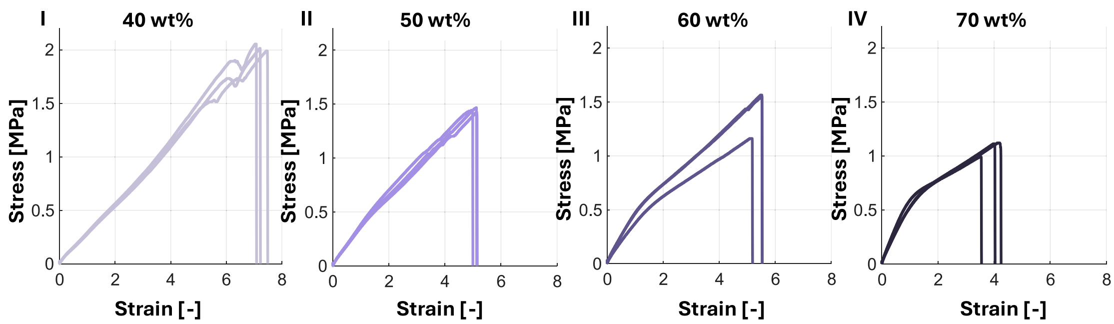

Figure 4. Break test results of dog-bone-shaped specimens made of DragonSkin-10 silicone filled with NdFeB hard magnetic microparticles at different concentrations: (I) 40 wt%, (II) 50 wt%, (III) 60 wt%, and (IV) 70 wt%. Each plot shows the stress–strain response of three independent samples subjected to a single uniaxial tensile test until failure. As the filler content increases, the composites exhibit increased stiffness and a marked reduction in elongation at break, indicating increased brittleness.

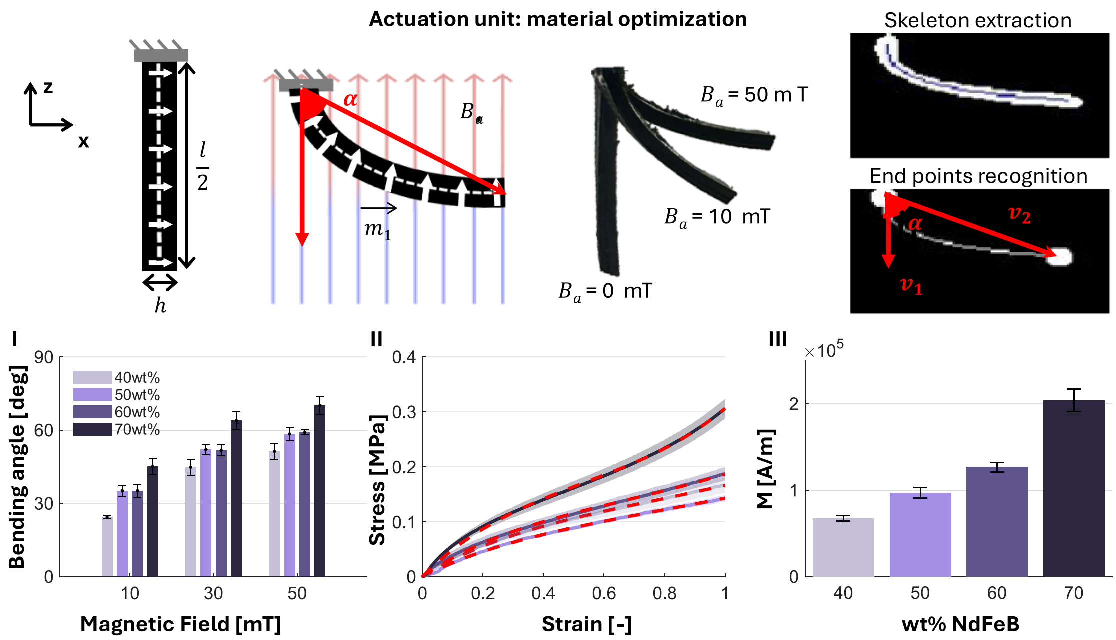

Figure 5. The mechanical and magnetic properties of DragonSkin-10 at 40 wt%, 50 wt%, 60 wt%, and 70 wt% magnetic particle concentrations were analyzed to assess the best compromise between manufacturability and bending capabilities of the actuation units. (I) Comparison of the bending angle tests. For each configuration, the bending performance was evaluated by capturing and analyzing MATLAB images of the actuated units under different magnetic fields. Skeleton extraction was applied to the images to identify the endpoints of the structure and calculate the bending angle α. Additionally, for each configuration: (II) cyclic stress–strain data were measured using an Instron testing machine, and (III) magnetization values were evaluated using a vibrating sample magnetometer.

3.2. Artificial trunk

Tests conducted on trunk prototypes incorporating 1 mm thick bending units showed that the concave design achieved a trunk volume change of 3.04 ± 0.12 cm^3, corresponding to 17.4% of the initial volume (V_0), whereas the convex design produced a volume change of 0.88 ± 0.01 cm^3, corresponding to 5.04% of V_0, demonstrating the superior performance of the concave configuration. Experimental tests carried out on the prototype with 1 mm thick bending units incorporating a groove along the bending line showed a trunk volume change of 3.8 ± 0.03 cm^3 (21.7% of V_0). Finally, tests conducted on trunk prototypes incorporating 2 mm thick bending units with the groove enabled a height increase of Δh = 1.286 ± 0.045 cm, corresponding to a trunk volume change of 7.70 ± 0.26 cm^3, equivalent to 43.9% of V_0 (supplementary video 3: volume-change assessment for proboscis design). This result is also in good agreement with the theoretical predictions, with a relative error of about 2.4% between the analytical model (45%) and the experiments (43.9%).

3.3. Performance characterization

Upon full proboscis deployment, the worm-inspired structure reaches a final body length of 2.5 times its initial length, closely mimicking the elongation capabilities of real worms (figures 6(A)–(II) and (B)–(II)). During tests, displacement occurred primarily

Table 3. Ogden parameters for DragoSkin-10 at different NdFeB particles concentrations (i.e 40 wt%, 50 wt%, 60 wt%, and 70 wt%).

DragonSkin-10			
40 wt%		50 wt%	
$\mu_1 = 1.54$ E + 00	$\alpha_1 = 1.14$ E + 01	$\mu_1 = 3.56$ E + 03	$\alpha_1 = 5.07$ E + 00
$\mu_2 = 1.96$ E + 07	$\alpha_2 = 1.03$ E-02	$\mu_2 = 7.34$ E + 02	$\alpha_2 = 0.001$ E + 00
$\mu_3 = 5.07$ E + 03	$\alpha_3 = 4.46$ E + 00	$\mu_3 = 3.35$ E + 07	$\alpha_3 = 5.13$ E-03
$R^2 = 0.99$		$R^2 = 0.99$	
60 wt%		70 wt%	
$\mu_1 = 1.74$ E + 07	$\alpha_1 = 0.12$ E-01	$\mu_1 = 5.19$ E + 02	$\alpha_1 = 8.73$ E + 00
$\mu_2 = 3.90$ E-07	$\alpha_2 = 2.93$ E + 01	$\mu_2 = 9.580$ E + 07	$\alpha_2 = 3.60$ E-02
$\mu_3 = 3.34$ E + 03	$\alpha_3 = 5.32$ E + 00	$\mu_3 = 1.49$ E + 05	$\alpha_3 = 1.84$ E-01
$R^2 = 0.99$		$R^2 = 0.99$	

along the Z-axis, with negligible lateral movements (<1 mm) in the prototypes without passive hyperelastic strips. In contrast, the addition of hyperelastic strips resulted in significantly larger lateral oscillations, reaching up to 5.06 ± 0.04 mm during deployment and 6.5 ± 0.05 mm during retraction. This behavior can be attributed to the elastic restoring forces generated by the strips; while they enable the retraction of the proboscis, they likely introduced asymmetric stresses during actuation, possibly as a result of geometric or material imperfections introduced during manufacturing.

As shown in figures 6(A)–(III) and (B)–(III), at the beginning of the actuation, the pressure increased sharply, marking the onset of proboscis displacement. Beyond this point, the pressure curve leveled off, even as the magnetic field strength continued to rise. This stabilization likely occurred because the fluid was no longer confined within the trunk but was progressively transferred into the extending proboscis, where material eversion accommodated the fluid without further pressure build-up. While the worm-inspired structure without retractor muscles reached a maximum pressure value of 2.53 ± 0.07 kPa, the structure with retractor muscles required higher fluid compression to overcome the resistance of the hyperelastic strips. Indeed, the maximum fluid pressure value was 2.94 ± 0.01 kPa. At low proboscis displacements, the force response of the two configurations (with and without hyperelastic strips) was comparable, with the latter even showing slightly higher values (maximum force of 1024.97 ± 63 mN and 956.15 ± 28.3 mN for the prototypes without and with retractor muscles, respectively; figures 6(A)–(V) and (B)–(V)).

At larger displacements, however, the trend was reversed. As the elongation increased, the hyperelastic strips underwent significant stretching, which considerably amplified their restoring forces. This strain-stiffening effect, intrinsic to hyperelastic materials, progressively opposed the actuation, thereby reducing the net force output of the prototypes with strips relative to those without strips. For the prototype without strips, at a displacement of 40 mm (i.e. 5 mm before the maximum extension), the residual force was interpreted as the force required to counterbalance the force exerted by the strips while still allowing proboscis eversion.

As expected, the internal pressure exhibited a decreasing trend as the proboscis displacement increased, reflecting the redistribution of fluid from the confined trunk into the extended proboscis. It is worth noting that when proboscis deployment was complete, the pressure value was almost equivalent to the maximum pressure recorded during previous unconstrained displacement tests.

In this work, the maximum magnetic field applied is limited by the capabilities of the EPM used in the experiments, with the prototype positioned at 5 mm from the magnet. Although higher field intensities cannot be achieved under the current setup, it should be noted that the applied field is already relatively strong. Additionally, extreme curvature of the bending units is limited because excessive bending can lead to self-contact between adjacent units, mechanically restricting further motion and reducing effective actuation. As demonstrated by the model described in section 2.3—artificial trunk, and schematized in figure 3(B), in this concave configuration the bending units form a circular arc with radius r_{cc} when actuated, and a bending limit is reached when the units begin to interfere with each other beyond a certain internal deflection.

Excessive bending could also compromise the overall structural stability. In this respect, sufficient stiffness of the bottom base is essential. Moreover, the presence of a longitudinal groove along the median line of the bending units helps mitigate potential buckling phenomena by promoting controlled bending in the desired direction while suppressing unintended deformations.

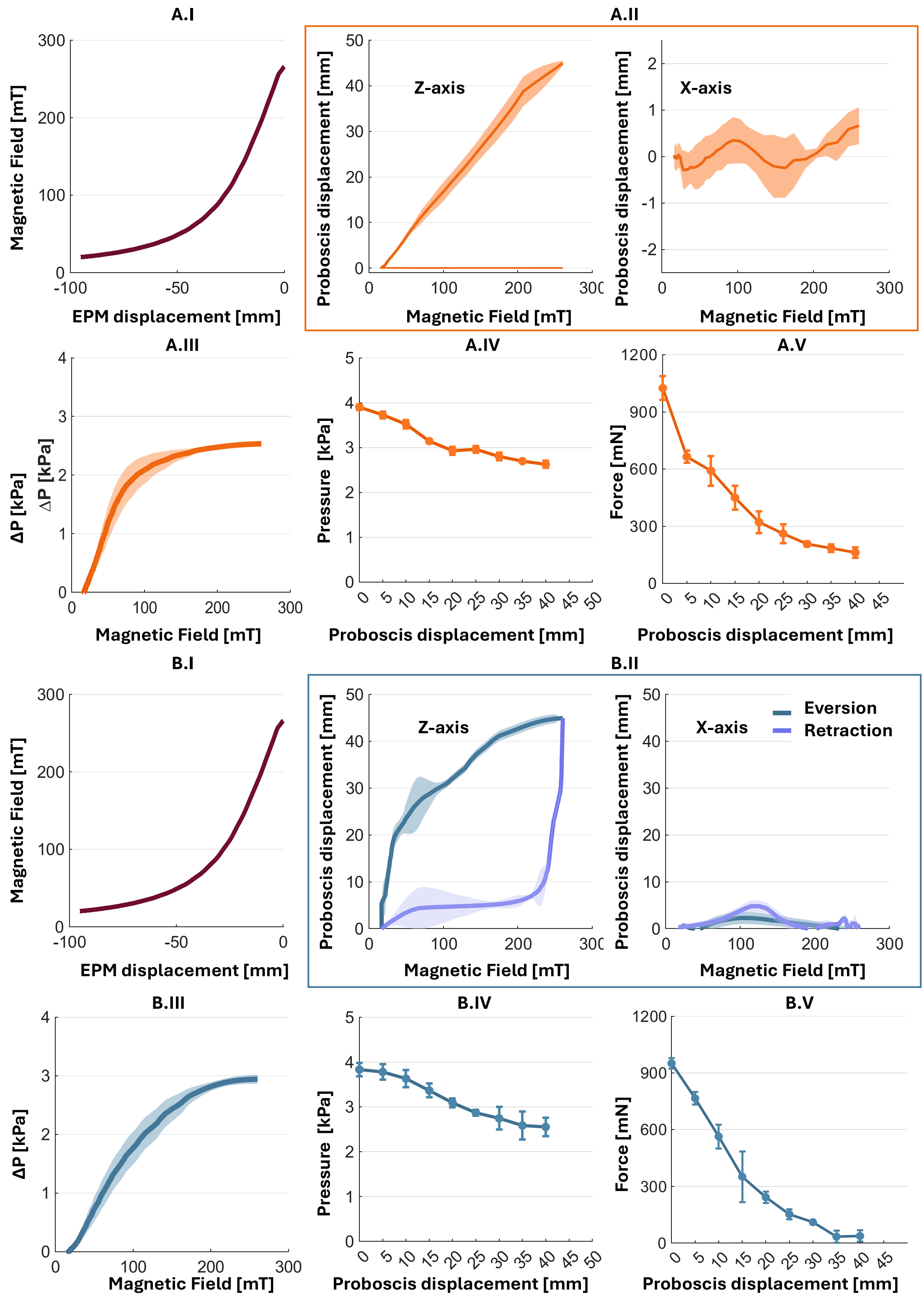

Figure 6. Performance of the worm-inspired structure without (A) and with (B) passive retractor muscles. (I) Magnetic field intensity applied along the Z-axis by adjusting the EPM pose, ranging from 10 mT (r = 95 mm) to 250 mT (r = 5 mm). (II) Deployment controllability: the proboscis tip was tracked along the Z- and X-axes (zoomed view), using the experimental setup in figure S1(A) of the supplementary materials. (III) Fluid pressure variation during free proboscis deployment. (IV) Fluid pressure variation, while also measuring (V) the tip force at different proboscis elongations, using the experimental setup in figure S1(B) of the supplementary materials.

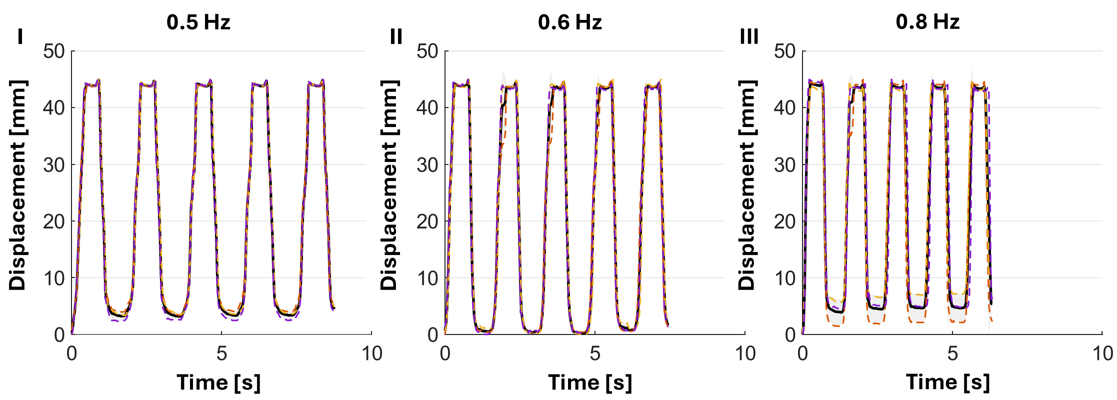

Figure 7. Tip displacement of the proboscis during cyclic actuation at different excitation frequencies: (I) 0.5 Hz, (II) 0.6 Hz, and (III) 0.8 Hz. The tracked displacement over time shows repeatable elongation–retraction cycles with peak displacements of approximately 45 mm. Minor residual offsets after retraction are visible at some frequencies, likely due to fluid redistribution and viscoelastic effects within the soft structure.

3.4. Dynamic characterization

The cyclic actuation behavior of the system was evaluated at three different magnet movement frequencies (0.5 Hz, 0.6 Hz, and 0.8 Hz), while the tip displacement of the proboscis was tracked over time (figure 7 and supplementary video 4: dynamic response of the magnetically driven deployable structure). The results show a consistent and repeatable response across all tested frequencies, with the device reaching peak displacements of approximately 45 mm during each cycle.

Overall, the system exhibits stable periodic behavior throughout the actuation cycles. A slight residual displacement can be observed at the end of some cycles, indicating that the proboscis does not always fully retract to its initial position. This small offset is likely related to fluid redistribution and viscoelastic effects within the soft structure. Nevertheless, the deviation remains limited and does not significantly affect the repeatability of the actuation, confirming the robustness of the proposed magneto-fluidic mechanism over the investigated frequency range.

3.5. Potential applications

The system's ability to generate linear movement, combined with its fully polymeric, biocompatible structure and high deformability, makes it a promising platform for a broad range of applications. These include medical use, agritech, and environmental exploration, where gentle interaction with delicate elements such as biological tissues, plants, or fragile ecosystems is required. Potential applications were explored in which the bioinspired system could be employed for the projection or controlled release of substances such as drugs, fertilizers, nutrients, or seeds. A substance delivery scenario was simulated in which a small capsule was placed at the proboscis tip (supplementary video 5: potential applications: delivery scenario and payload ejection). In one configuration (figure 8(A)), the magnetic field was increased gradually by controlling the motion of the EPM through the robotic positioning system operated in open loop (EPM speed = 50 mm s^{-1}), and the capsule was fixed at the tip of the structure, mimicking a targeted and gradual release. In the second configuration (figure 8(B)), the application of the magnetic field, again regulated in open loop via the EPM motion (EPM speed = 100 mm s^{-1}), induced a sudden extension and dynamic acceleration of the proboscis tip, resulting in payload ballistic ejection.

4. Conclusions and discussions

Soft linear actuators are mainly inflatable systems in which elongation is achieved through direct pressurization. The main objective of this work was to develop a novel soft actuation strategy, in which linear motion is enabled by a bioinspired, magnetically driven fluidic transmission mechanism. Different solutions for fluidic transmission have been reported in the literature [50–54], often relying on pneumatic inflation of internal chambers. Upon pressurization, these systems experience radial expansion, typically constrained by rigid external elements to favor axial motion. An example inspired by Sipuncula worms is the solution proposed by Filogna *et al* [25], which achieves an elongation ratio of approximately 1.5, compared to the 2.5 reached by our system. Moreover, that approach relies on tethered pneumatics and incorporates a rigid case to constrain the radial deformation of an air-driven pneumatic chamber, typically operated at pressures on the order of 140 kPa (see table 1). In contrast, the present solution achieves an elongation ratio of 2.5 through a wireless and entirely soft architecture. This is enabled by a tailored distribution of material stiffness, which intrinsically regulates deformation direction and eliminates the need for rigid constraints, while actuation is driven by magnetic fields of approximately 250 mT.

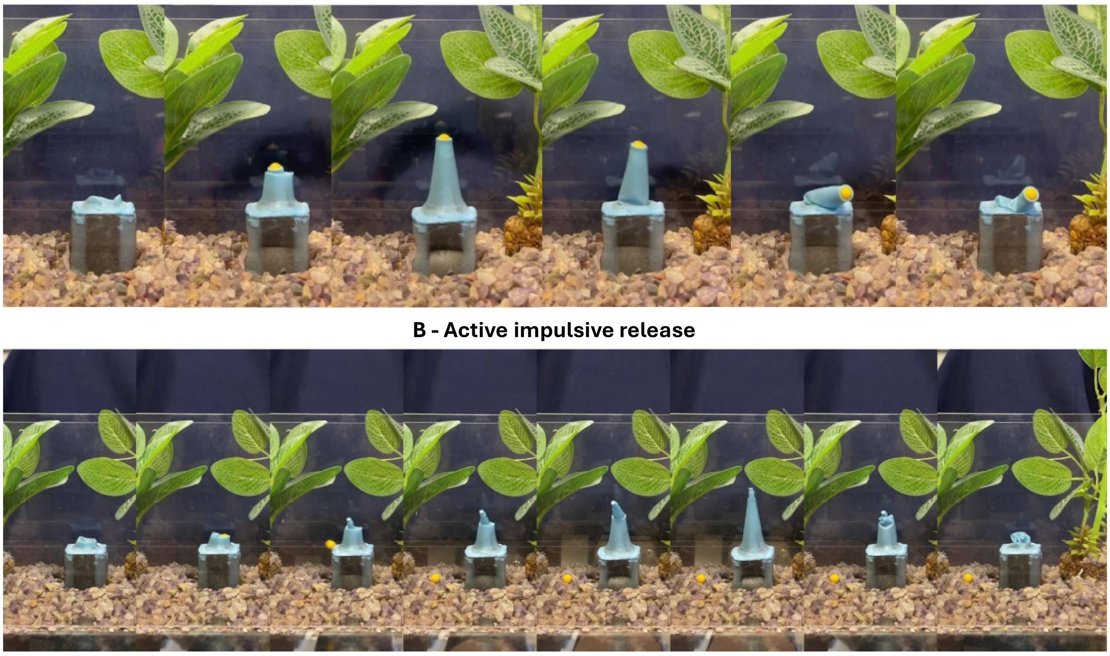

Figure 8. Sequential snapshots illustrating two distinct substance release modalities of the worm-inspired smart structure. (A) Targeted and localized release: the capsule remains attached at the tip while the payload is gradually released. (B) Active impulsive release: the capsule, resting freely on the tip, is rapidly ejected upon sudden extension induced by a sharp increase in the magnetic field.

Similarly, other state-of-the-art systems inspired by the protrusion mechanism of Sipuncula worms rely on pneumatic actuation and therefore require large external pumps to inflate the everting chambers [26, 27, 32]. Although these approaches can achieve extremely large elongations (up to 700%) and high speeds (on the order of 10 m s^{-1}), their reliance on external pneumatic devices inherently limits their applicability in specific contexts. For instance, the presence of pneumatic lines poses significant challenges in environments that must remain sealed or sterile, as they represent potential sources of leakage and contamination. Additionally, their reliance on external drivers prevents the implementation of fully untethered actuation strategies, while in solutions with onboard actuation, it is difficult to miniaturize the system to dimensions below the order of tens of centimeters [34]. As a result, the use of such devices is constrained in compact, sealed, or difficult-to-access environments. In contrast, the proposed magnetically driven soft actuator enables fluidic transmission through untethered actuation, featuring a magneto-responsive trunk and a fully passive proboscis inspired by the protrusion mechanism exhibited by Sipuncula worms.

After identifying the optimal combination of silicone material and magnetic particle concentration, experimental results demonstrated that the soft structure successfully achieves both protrusion and retraction, mimicking the behavior of its biological counterpart. Retraction was achieved by means of two hyperelastic strips, attached at one end to the proboscis and the other end to the trunk base. Upon increasing the magnetic field, the soft robotic structure elongated up to 2.5 times the trunk's initial resting length, while the elastic strips exhibited an elongation ratio of up to 4.5, owing to their intrinsic softness. When the magnetic field was reduced, the magnetic bending units recovered their initial configuration, and the spring-like behavior of the strips facilitated the retraction of the proboscis into the trunk.

Although the integration of hyperelastic strips introduced slight asymmetries (and consequently minor reductions in stability) their presence was crucial to achieve reliable retraction. Indeed, negative-pressure-driven retraction alone could not guarantee effective functioning.

The relationship between the bending of the trunk actuation units and the resulting fluid displacement was described through a mathematical model. The model estimated a volume change of 45%, while experimental measurements yielded 7.70 ± 0.26 cm^3, corresponding to a 43.9%volume change. This level of agreement supports the model validity under the tested conditions.

Experimental tests demonstrated that the magnetically induced bending motion of the actuation units can be effectively converted into the linear displacement of a fully passive soft proboscis, achieving output forces of up to 1 N. In contrast to state-of-the-art systems, where magnetic fields are predominantly employed to enable inchworm-like locomotion rather than controlled elongation [40, 45, 46], the proposed architecture achieves axial deployment through the synergistic coupling of magnetic actuation and fluid-mediated pressure transmission. Additionally, embedding magnetic particles within the soft matrix eliminates the need for rigid components, such as discrete magnets integrated into the body structure [15, 36]. This hybrid mechanism enables an efficient conversion of magnetically induced bending into hydraulic pressure. As a result, the system generates higher tip forces than previously reported magnetically driven systems, reaching up to 1 N, compared with 0.28 N in [36], 0.06 N in [16], 0.29 N in [46], and 0.8 N in [47] (see table 1). Furthermore, devices of comparable size relying on direct magnetic actuation typically achieve displacements of only about 5 mm [47], whereas the proposed magneto-fluidic transmission mechanism enables strokes of up to 45 mm, corresponding to an approximately nine-fold increase in displacement. These characteristics make the proposed approach particularly suitable for operation in constrained and delicate environments, where conventional tethered soft robots face significant limitations.

Despite the promising performance achieved, several factors currently define the operational limits of the proposed system. One aspect concerns the working fluid used inside the trunk. In the present prototype, water was employed as the internal fluid due to its simplicity and availability. However, water can partially diffuse through silicone over time and exhibits a small but non-negligible compressibility. These effects may slightly reduce the efficiency of fluid transmission during repeated actuation cycles. Future work will therefore investigate alternative fluids with lower permeability and different compressibility to further improve actuation efficiency and long-term stability of the system. In addition, the magnetic composite used for the actuation units requires a compromise between magnetic responsiveness and mechanical compliance. Increasing the concentration of NdFeB particles enhances magnetization and bending torque but also increases the stiffness of the composite, which can limit deformation capability and potentially affect long-term durability under repeated actuation cycles. Finally, asymmetries in the actuation behavior may arise from geometric or material imperfections introduced during the manufacturing process, such as small variations in particle dispersion, layer thickness, or bonding between components, which may affect the symmetry of the system. At present, the system is fabricated at the centimeter scale, largely due to manufacturing constraints. In the future, the adoption of advanced additive manufacturing techniques may enable further miniaturization, allowing the device to reach dimensions closer to those of the real worm and paving the way for applications in different fields.

Acknowledgment

This work was supported by the European project MAPWORMS—Mimicking Adaptation and Plasticity in WORMS Grant Agreement 101046846 (www.mapworms.eu).

Data availability statement

The data that support the findings of this study will be openly available following an embargo at the following URL/DOI: https://zenodo.org/communities/mapworms/records?q=&l=list&p=1&s=10&sort=newest [55].

Conflict of interest

The authors declare no conflict of interest.

Author contributions

Ilaria Cedrola 0009-0008-5152-0432
Conceptualization (lead), Data curation (lead), Investigation (lead), Methodology (lead), Validation (lead), Visualization (lead), Writing – original draft (lead), Writing – review & editing (lead)

Sabina Maglio 0000-0002-7922-5506
Data curation (supporting), Methodology (supporting)

Mohammad Hasan Dad Ansari 0000-0002-8450-1931
Data curation (supporting), Methodology (supporting)

Arianna Menciassi 0000-0001-6348-1081
Conceptualization (lead), Funding acquisition (lead), Supervision (lead), Writing – review & editing (lead)

Linda Paternò 0000-0002-6318-4033
Conceptualization (lead), Funding acquisition (lead), Supervision (lead), Writing – review & editing (lead)

References

[1] Sitti M 2021 Physical intelligence as a new paradigm *Extreme Mech. Lett.* **46** 101340

[2] Kortman V G, Mazzolai B, Sakes A and Jovanova J 2025 Perspectives on intelligence in soft robotics *Adv. Intell. Syst.* **7** 2400294

[3] Mengaldo G, Renda F, Brunton S L, Bächer M, Calisti M, Duriez C, Chirikjian G S and Laschi C 2022 A concise guide to modelling the physics of embodied intelligence in soft robotics *Nat. Rev. Phys.* **4** 595–610

[4] Ilami M, Bagheri H, Ahmed R, Skowronek E O and Marvi H 2021 Materials, actuators, and sensors for soft bioinspired robots *Adv. Mater.* **33** 2003139

[5] Ahmed F, Waqas M, Jawed B, Soomro A M, Kumar S, Hina A, Khan U, Kim K H and Choi K H 2022 Decade of bio-inspired soft robots: a review *Smart Mater. Struct.* **31** 073002

[6] Rus D and Tolley M T 2015 Design, fabrication and control of soft robots *Nature* **521** 467–75

[7] Kim S, Laschi C and Trimmer B 2013 Soft robotics: a bioinspired evolution in robotics *Trends Biotechnol.* **31** 287–94

[8] Ellers O, Ellers K-I, Johnson A S, Po T, Heydari S, Kanso E and McHenry M J 2024 Soft skeletons transmit force with variable gearing *J. Exp. Biol.* **227** jeb246901

[9] Zamanian A H and Voltzow J 2024 Soft robots and soft bodies: biological insights into the structure and function of fluidic soft robots *Bioinspir. Biomim.* **20** 013001

[10] Du T, Sun L and Wan J 2022 A worm-like crawling soft robot with pneumatic actuators based on selective laser sintering of TPU powder *Biomimetics* **7** 205

[11] Das R, Babu S P M, Visentin F, Palagi S and Mazzolai B 2023 An earthworm-like modular soft robot for locomotion in multi-terrain environments *Sci. Rep.* **13** 1571

[12] Zhao Y, Huang H, Yuan W, Liu X and Cao C C 2024 Worm-inspired, untethered, soft crawling robots for pipe inspections *Soft Robot.* **11** 639–49

[13] Xiong Q, Ang B W K, Jin T, Ambrose J W and Yeow R C H 2023 Earthworm-inspired multi-material, adaptive strain-limiting, hybrid actuators for soft robots *Adv. Intell. Syst.* **5** 2200346

[14] Liu J, Li P, Huang Z, Liu H and Huang T 2025 Earthworm-inspired multimodal pneumatic continuous soft robot enhanced by winding transmission *Cyborg Bionics Syst.* **6** 0204

[15] Niu H, Feng R, Xie Y, Jiang B, Sheng Y, Yu Y, Baoyin H and Zeng X 2021 MagWorm: a biomimetic magnet embedded worm-like soft robot *Soft Robot.* **8** 507–18

[16] Joyee E B and Pan Y 2019 A fully three-dimensional printed inchworm-inspired soft robot with magnetic actuation *Soft Robot.* **6** 333–45

[17] Ze Q, Wu S, Nishikawa J, Dai J, Sun Y, Leanza S, Zemelka C, Novelino L S, Paulino G H and Zhao R R 2022 Soft robotic origami crawler *Sci. Adv.* **8** eabm7834

[18] You T L, Philamore H and Matsuno F 2021 A magneto-active elastomer crawler with peristaltic and caterpillar locomotion patterns *Actuators* **10** 74

[19] Muff L F, Mills A S, Riddle S, Buclin V, Roulin A, Chiel H J, Quinn R D, Weder C and Daltorio K A 2023 Modular design of a polymer-bilayer-based mechanically compliant worm-like robot *Adv. Mater.* **35** 2210409

[20] Wu S, Hong Y, Zhao Y, Yin J and Zhu Y 2023 Caterpillar-inspired soft crawling robot with distributed programmable thermal actuation *Sci. Adv.* **9** eadf8014

[21] Onal C D, Wood R J and Rus D 2013 An origami-inspired approach to worm robots *IEEE/ASME Trans. Mechatronics* **18** 430–8

[22] Xu L *et al* 2022 Locomotion of an untethered, worm-inspired soft robot driven by a shape-memory alloy skeleton *Sci. Rep.* **12** 12392

[23] Lu X, Wang K and Hu T 2020 Development of an annelid-like peristaltic crawling soft robot using dielectric elastomer actuators *Bioinspir. Biomim.* **15** 046012

[24] Filogna S, Iacovacci V, Vecchi F, Musco L and Menciassi A 2021 Protrusion mechanism study in sipunculid worms as model for developing bio-inspired linear actuators *Bioinspir. Biomim.* **16** 026008

[25] Filogna S, Paternò L, Vecchi F, Musco L, Iacovacci V and Menciassi A 2023 A bioinspired fluid-filled soft linear actuator *Soft Robot.* **10** 454–66

[26] Hawkes E W, Blumenschein L H, Greer J D and Okamura A M 2017 A soft robot that navigates its environment through growth *Sci. Robot.* **2** eaan3028

[27] Greer J D, Morimoto T K, Okamura A M and Hawkes E W 2019 A soft, steerable continuum robot that grows via tip extension *Soft Robot.* **6** 95–108

[28] Berthet-Rayne P, Sadati S M H, Petrou G, Patel N, Giannarou S, Leff D R and Bergeles C 2021 MAMMOBOT: a miniature steerable soft growing robot for early breast cancer detection *IEEE Robot. Autom. Lett.* **6** 5056–63

[29] Luong J, Glick P, Ong A, deVries M S, Sandin S, Hawkes E W and Tolley M T 2019 Eversion and retraction of a soft robot towards the exploration of coral reefs *2019 2nd IEEE Int. Conf. on Soft Robotics (Robosoft)* pp 801–7

[30] Talas S K, Baydere B A, Altinsoy T, Tutcu C and Samur E 2020 Design and development of a growing pneumatic soft robot *Soft Robot.* **7** 521–33

[31] Shi J, Borvorntanajanya K, Chen K, Franco E and Baena F R 2025 Design, control, and evaluation of a novel soft everting robot for colonoscopy *IEEE Trans. Robot.* **41** 4843–59

[32] Davy J, Greenidge N J, Kim S, Tinsley L J, Lloyd P, Chandler J H, Harris R A, Morimoto T K and Valdastri P 2024 Vine robots with magnetic skin for surgical navigations *IEEE Robot. Autom. Lett.* **9** 6888–95

[33] Blumenschein L H, Coad M M, Haggerty D A, Okamura A M and Hawkes E W 2020 Design, modeling, control, and application of everting vine robots *Front. Robot. AI* **7** 548266

[34] Perez N G B and Coad M M 2022 Self-propelled soft everting toroidal robot for navigation and climbing in confined spaces *2022 IEEE/RSJ Int. Conf. on Intelligent Robots and Systems (IROS)* pp 5409–15

[35] Soto F, Karshalev E, Zhang F, Esteban Fernandez de Avila B, Nourhani A and Wang J 2022 Smart materials for microrobots *Chem. Rev.* **122** 5365–403

[36] Jin Y, Li J, Liu S, Cao G and Liu J 2023 A worm-inspired robot based on origami structures driven by the magnetic field *Bioinspir. Biomim.* **18** 046008

[37] Li Z, Lai Y P and Diller E 2024 3D printing of multilayer magnetic miniature soft robots with programmable magnetization *Adv. Intell. Syst.* **6** 2300052

[38] Dong Y, Wang L, Xia N, Yang Z, Zhang C, Pan C, Jin D, Zhang J, Majidi C and Zhang L 2022 Untethered small-scale magnetic soft robot with programmable magnetization and integrated multifunctional modules *Sci. Adv.* **8** eabn8932

[39] Tang D, Zhang C, Sun H, Dai H, Xie J, Fu J and Zhao P 2021 Origami-inspired magnetic-driven soft actuators with programmable designs and multiple applications *Nano Energy* **89** 106424

[40] Li S, Li R, Wang J, Meng X and Xie H 2024 Inchworm-like soft robot with anisotropic magnetization for untethered crawling and manipulating *2024 IEEE Int. Conf. on Robotics and Biomimetics (ROBIO)* pp 553–8

[41] Yi S *et al* 2022 High-throughput fabrication of soft magneto-origami machines *Nat. Commun.* **13** 4177

[42] Hu W, Lum G Z, Mastrangeli M and Sitti M 2018 Small-scale soft-bodied robot with multimodal locomotion *Nature* **554** 81–85

[43] Xu C, Yang Z, Tan S W K, Li J and Lum G Z 2022 Magnetic miniature actuators with six-degrees-of-freedom multimodal soft-bodied locomotion *Adv. Intell. Syst.* **4** 2100259

[44] Ijaz S, Li H, Hoang M C, Kim C-S, Bang D, Choi E and Park J-O 2020 Magnetically actuated miniature walking soft robot based on chained magnetic microparticles-embedded elastomer *Sens. Actuators A* **301** 111707

[45] Shen H, Cai S, Wang Z, Yuan Z, Yu H and Yang W 2023 A programmable inchworm-inspired soft robot powered by a rotating magnetic field *J. Bionics Eng.* **20** 506–14

[46] Xia D, Zhang L, Nong W, Duan Q and Ding J 2025 3D-printed soft bionic inchworm robot powered by magnetic force *Biomimetics* **10** 202

[47] Lin D, Yang F, Gong D and Li R 2023 Bio-inspired magnetic-driven folded diaphragm for biomimetic robot *Nat. Commun.* **14** 163
[48] Ansari M H D, Iacovacci V, Pane S, Ourak M, Borghesan G, Tamadon I, Vander Poorten E and Menciassi A 2023 3D printing of small-scale soft robots with programmable magnetization *Adv. Funct. Mater.* **33** 2211918
[49] Petruska A J and Abbott J J 2013 Optimal permanent-magnet geometries for dipole field approximation *IEEE Trans. Magn.* **49** 811–9
[50] Zhang J, Wang T, Wang J, Wang M Y, Li B, Zhang J X J and Hong J 2020 Geometric confined pneumatic soft–rigid hybrid actuators *Soft Robot.* **7** 574–82
[51] Hashem R, Stommel M, Cheng L K and Xu W 2021 Design and characterization of a bellows-driven soft pneumatic actuator *IEEE/ASME Trans. Mechatronics* **26** 2327–38
[52] Zhang Z, Chen G, Wu H, Kong L and Wang H 2020 A pneumatic/cable-driven hybrid linear actuator with combined structure of origami chambers and deployable mechanism *IEEE Robot. Autom. Lett.* **5** 3564–71
[53] Paternò L, Tortora G and Menciassi A 2018 Hybrid soft–rigid actuators for minimally invasive surgery *Soft Robot.* **5** 783–99
[54] Gorissen B, Reynaerts D, Konishi S, Yoshida K, Kim J-W and De Volder M 2017 Elastic inflatable actuators for soft robotic applications *Adv. Mater.* **29** 1604977
[55] Available at: (https://zenodo.org/communities/mapworms/records?q=&l=list&p=1&s=10&sort=newest)